

Cite this: *RSC Adv.*, 2019, 9, 11046

# Ultrafine nanoparticles of W-doped SnO<sub>2</sub> for durable H<sub>2</sub>S sensors with fast response and recovery†

Pengjian Wang,<sup>ab</sup> Junfeng Hui,<sup>a</sup> Tingbiao Yuan,<sup>b</sup> Peng Chen,<sup>c</sup> Yue Su,<sup>c</sup> Wenjie Liang,<sup>c</sup> Fulin Chen,<sup>d</sup> Xiaoyan Zheng,<sup>\*ad</sup> Yuxin Zhao<sup>de</sup> and Shi Hu<sup>\*b</sup>

Ultrafine nanoparticles of W-doped SnO<sub>2</sub> with an average diameter of 6 nm were fabricated *via* a facile hydrothermal method. The material shows a reduced particle size and enhanced response to H<sub>2</sub>S gas as compared to the pristine SnO<sub>2</sub> nanoparticles. The detection limit can be down to 100 ppb while the response time and recovery time of the 5%-doped one are reduced to 17 s and 7 s respectively. In addition, the material shows impressive long-term stability of the response through 40 cycles of injection with 10 ppm H<sub>2</sub>S, which is attractive for designing a durable hydrogen sulfide sensor. The doping of W results in the reduction of size and modification of the electronic band structure of SnO<sub>2</sub>, which reduces the response time and recovery time and further improves the sensing durability of the materials.

Received 4th February 2019  
Accepted 28th March 2019

DOI: 10.1039/c9ra00944b

rsc.li/rsc-advances

## 1. Introduction

With the growth of global oil & gas exploration as well as drying up of high-quality light sweet crude, more sour fields with high sulfur content have to be developed. Therefore, the leakage incidents of highly toxic gas hydrogen sulfide (H<sub>2</sub>S) during well drilling, pipeline transportation, oil refinement and final discharge have remarkably increased over the past decades. In 2003, the blowout of sour-gas wells in southwestern China, described as the worst accidental H<sub>2</sub>S emission in history, caused 243 deaths and 64 000 residents were evacuated from the exposure area, greatly harming the safety of civilians, as well as its further comprehensive influence over time.<sup>1</sup> In addition to its health issues, the flammable nature of H<sub>2</sub>S could also threaten public security owing to the risk of fire and explosion.<sup>2</sup> Therefore, the development of efficient and robust H<sub>2</sub>S sensors

for the timely and reliable detection under practical harsh conditions is highly imperative.

To date, various gas sensors have been applied in H<sub>2</sub>S gas monitoring, such as colorimetric assay,<sup>3</sup> chemoresistive sensors,<sup>4</sup> electrochemical sensors,<sup>5</sup> piezoelectric sensors,<sup>6</sup> optical sensors and conducting polymeric sensors,<sup>7,8</sup> *etc.* Among these alternatives, semiconducting metal oxide (SMO) sensors are considered to be the most economical, convenient and efficient with typical detection range in ppm levels.<sup>9</sup> Their working principle is based on the electrical variation introduced by the diffusion or chemical reaction of gases/vapors in the coated or deposited sensitive layer. Thus the performance of this solution depends largely on sensing materials. To meet the demands of actual applications, researchers have devoted significant attention to develop H<sub>2</sub>S sensitive materials, particularly molybdenum trioxide,<sup>4</sup> tungsten trioxide,<sup>10</sup> cupric oxide,<sup>11</sup> zinc oxide<sup>12</sup> and stannic oxide<sup>13</sup> with a lot of “debugging” possibilities (*i.e.* size reduction, surface decoration, hetero-junction, composite formation, *etc.*) on purpose.<sup>8,14–16</sup> These candidates have shown many advantages, including improved surface catalytic activation, high electron mobility and appropriate contact potential at the interface between components. For example, detection limits of ppb and ppm of H<sub>2</sub>S were demonstrated using graphene flakes/WO<sub>3</sub> nanofibers and Cu–ZnO nanowires, respectively.<sup>9,17</sup> However, there still exist several unaddressed scientific and technical challenges. One primary challenge is instability issues of the contact state of sensing interface caused by physical and chemical degrading processes owing to the complex humid environment.<sup>18</sup> The presence of acidic corrosive components, dirt particles in the atmosphere as well as intermittent thermal shock, usually cause the failure of elaborated surface functional groups and micro-/nano-

<sup>a</sup>Shaanxi Key Laboratory of Degradable Biomedical Materials, Shanxi R&D Center of Biomaterials and Fermentation Engineering, School of Chemical and Engineering, Northwest University, Xian, Shaanxi 710069, China. E-mail: zy129@126.com

<sup>b</sup>Department of Chemistry, School of Science, Tianjin Key Laboratory of Molecular Optoelectronic Science, Tianjin University, Tianjin 300072, China. E-mail: ryuchushi@gmail.com

<sup>c</sup>Beijing National Laboratory for Condensed Matter Physics, Beijing Key Laboratory for Nanomaterials and Nanodevices, Institute of Physics, Chinese Academy of Sciences, Beijing 100190, China

<sup>d</sup>College of Life Sciences, Northwest University, Xian, Shaanxi 710069, China

<sup>e</sup>State Key Laboratory of Safety and Control for Chemicals, SINOPEC Research Institute of Safety Engineering, No. 339, Songling Road, Laoshan District, Qingdao, Shandong 266071, China. E-mail: zhaoyuxin1@yeah.net

† Electronic supplementary information (ESI) available. See DOI: 10.1039/c9ra00944b



architectures during long-term cycling, which leads to loss of active sites and eventual fading of sensing capacity. Another challenge is two essential properties of sensing materials—high response sensitivity and high recovery rate—are contradictory. The strong bonding between target gas and sensing layer at lower concentrations could achieve high sensitivity and selectivity, but also make it harder to desorb gas molecules and hence resulting in sluggish recovery. This problem is particularly acute in “room-temperature” gas sensors, wherein recovery time ( $t_{50}$ : time taken for the sensor to recover within 50% of its initial baseline after removal of gas) is generally around several minutes or more with detection ranges of 1–20 ppm, which is insufficient to meet the actual requirement.<sup>19,20</sup> Finally, these challenges are compounded with the fact that the synthesis must be easily scaled up and easily integrated with electronics for real-world utilizations.

While there have been exciting progresses in addressing a subset of these challenges, few have sought to address all of these challenges simultaneously. Recently, non-carbon ultra-fine nanostructures with further reduced size of sub-10 nm as compared to traditional nanomaterials afford promising opportunities to address all of these challenges. Due to their significant decrease of the thickness, the percentage of surface atoms and active sites exposed can be greatly enhanced, making them highly favourable for surface-dominated adsorption-desorption mass transfer process and chemo-catalysis applications.<sup>21,22</sup> Another attractive feature of ultrathin nanomaterials is their unique electronic structures tenability.<sup>23</sup> Such external-stimuli sensitive nature allows us to fine tune their electronic properties in a desired manner at a highly controllable level *via* the use of reticular chemistry, such as chemical modification, doping, and hybridization. The electron confinement in ultrathin materials especially semiconductors, enable greatly compelling electronic properties and concomitant intrinsic bandgap variation, therefore rendering them appealing candidates for electronic device applications and fundamental condensed matter research.<sup>24,25</sup> Furthermore, to quantify the atomic thickness that may be attained with effective assembling of ultrathin film monolayers or porous constructs while offering them maximum mechanical flexibility and stability, making them suitable for the integration of reliable and highly flexible semiconductor electrodes in sensing applications.<sup>22,26</sup> It is worth noting that doping can effectively change the electronic structure of the SMOs. Thus, doping is the most commonly used methods to enhance the gas sensing performance of SMOs to certain gases. Tungsten, a member of the transition metals element, has a variety of oxidation states. It is expected to be an efficient doping material in the field of gas sensing applications. It has been realized that doping high-valent metal element can effectively improve the gas sensing properties of materials. In addition, the radius of tungsten ( $W^{6+}$ : 67 pm) is close to that of tin ( $Sn^{4+}$ : 71 pm), and hence  $W^{6+}$  can easily replace  $Sn^{4+}$  in theory.<sup>27</sup>

Herein, a facile hydrothermal method was demonstrated to grow ultrafine W-doped  $SnO_2$  nanoparticles (WS-NPs). As a proof of concept, the uniform distribution of well-decorated NPs without aggregation on SMO sensors and their potential

application toward  $H_2S$  monitoring were demonstrated. Taking advantage of large lateral size with ultrahigh specific surface area, more oxygen adsorption sites and ready gas accessibility, a great improvement in sensitivity and selectivity even toward ppb level of  $H_2S$  gas can be achieved. Principally,  $SnO_2$  nanoparticles with 5% W doping exhibited an ultra-fast response-recovery time sensing to 10 ppm  $H_2S$  at 260 °C. Furthermore, adsorption/desorption kinetic process on the surface of WS-NPs was also proposed. It is expected that these ultrafine NPs are promising for a real-time monitoring of trace  $H_2S$  in oil/gas platforms and refineries, as well as in manufacturing processes and fire-fighting.

## 2. Experimental procedure

### 2.1 Chemicals

Tin(II) chloride dihydrate ( $SnCl_2 \cdot 2H_2O$ ), absolute ethanol were purchased from Sinopharm Chemical Reagent Co. Ltd. Urea was purchased from Aladdin Chemical Reagent Co. Ltd. Tungsten hexachloride ( $WCl_6$ ) was purchased from Shanghai Macklin Biochemical Co. Ltd. All chemicals were used as received without further purification. Deionized water was used throughout the experiments.

### 2.2 Synthesis of materials

$SnO_2$  nanoparticles were synthesized by a facile hydrothermal process followed by calcination. In a typical synthesis procedure, 0.04 g of  $SnCl_2 \cdot 2H_2O$  and 0.01 g of urea were added into 40 ml of deionized water and the mixture was then stirred for 30 min to form a homogeneous solution. Afterward, the reaction solution was transferred to a 50 ml Teflon-lined stainless-steel autoclave and kept in an oven at 180 °C for 24 h. After naturally cooling down to room temperature, the product was collected by centrifugation, rinsed with distilled water and absolute ethanol for several times, and dried at 60 °C for 12 h. The obtained intermediate product was further calcinated at 500 °C for 2 h with a heating rate 5 °C  $min^{-1}$  to obtain the final product.

W-doped  $SnO_2$  nanoparticles were synthesized with a similar procedure as follows. First, an appropriate amount of  $WCl_6$  was added to 20 ml of absolute ethanol. After 5 min of stirring, 0.04 g of  $SnCl_2 \cdot 2H_2O$  and 0.01 g of urea were added into the homogeneous solution and then transferred into a 50 ml Teflon-lined autoclave which was sealed and kept at 180 °C for 24 h. The amount of  $WCl_6$  was calculated according to the atomic weight ratio:  $W/SnO_2 = 0\%, 1\%, 2.5\%, 5\%, 7.5\%, 10\%$ . After cooling down to room temperature, the solid products were collected using the same process described above and dried at 60 °C for 12 h. Finally, all samples were calcinated at 500 °C in air for 2 h before the following characterization. The pristine and W-doped  $SnO_2$  nanoparticles with different doping concentrations of 0, 1, 2.5, 5, 7.5, 10% were synthesized and labelled as WS-0, WS-1, WS-2.5, WS-5, WS-7.5 and WS-10, respectively.

### 2.3 Fabrication and measurement of gas sensors

The gas sensing property of the materials were tested by the following steps. First, the samples were mixed with terpineol and uniformly coated on the surface of alumina ceramic tube with a heating resistor of Ni-Cr alloy going through the hollow part of the ceramic tube and a pair of gold electrodes attached on the surface and connected by Pt wires.<sup>28</sup> The coated tube was left to age at 400 °C for 48 h to burn off the terpineol. The material became porous with the resistance stabilized during aging before it was tested on a computer-controlled gas-sensing system (WS-30A by Winson Electronics Co., Ltd., Zhengzhou, China). In the sensing test process, an appropriate bias voltage ( $V_c = 5$  V) was applied. The whole test environment was in the air atmosphere (12–17 °C) with a humidity level controlled at 30–40%.

The gas response is defined as  $R_a/R_g$  ( $R_a$  and  $R_g$  are the electric resistance of the sensors in air and in the target gas, respectively).<sup>29,30</sup> The response time ( $t_{res}$ ) is defined as the time for the resistance to reach 90% of the final stable output after the injection of target gas, while the recovery time ( $t_{rec}$ ) is defined as the time to fall to 10% of its maximum output after the target gas was discharged.<sup>14,28,31</sup>

## 3. Results and discussion

### 3.1 Morphology and structure

The crystal structure of all the samples were reflected by their XRD patterns with well-resolved diffraction peaks in the range from 20° to 80°. As shown in Fig. 1, all the peaks can be assigned to SnO<sub>2</sub> of cassiterite structure (JCPDS: 41-1445) and no diffraction peaks from the oxides of tungsten were detected for the W-doped SnO<sub>2</sub> up to the doping level of 10%. No sign of oxide of tungsten could be identified from this series of patterns, indicating good dispersion of tungsten in SnO<sub>2</sub> lattice, which could be attributed to the similar radius of Sn<sup>4+</sup> (71 pm) with W<sup>6+</sup> (67 pm). It should be noted that the size of the nanocrystallite shows a decreasing trend with the increase of doping level, as indicated by the widening of the diffraction

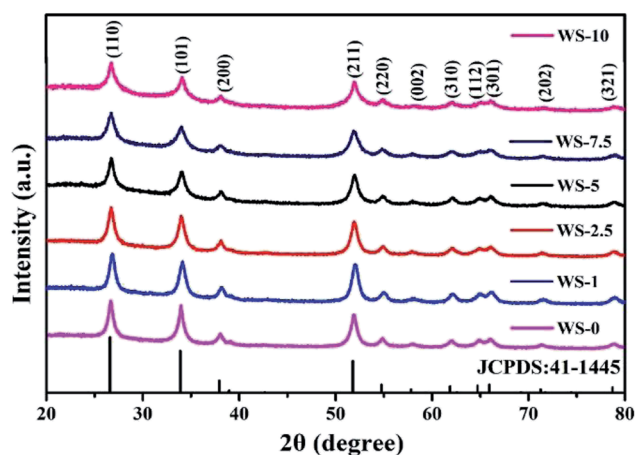


Fig. 1 XRD pattern of the pristine SnO<sub>2</sub> and W-doped SnO<sub>2</sub> nanoparticles with increasing doping level.

peaks. Applying Scherrer equation to the full width at half maximum (FWHM) of (110) peaks yields a crystal size of 15.6 nm for undoped SnO<sub>2</sub> against 7.6 nm for 5% W-doped SnO<sub>2</sub> and 6.6 nm for 10% W-doped SnO<sub>2</sub>. Similar results can be obtained with 14.8 nm against 7.1 nm and 6.6 nm for (101) diffraction and 12.6 nm against 7.1 nm and 6.1 nm for (211) diffractions. It is worth noting that, the pristine SnO<sub>2</sub> after hydrothermal synthesis contains SnO (JCPDS card no. 85-0712), as is shown in Fig. S1.† It is eliminated through further annealing process while the W-doped sample completely converts to SnO<sub>2</sub> even before the annealing. This could be attributed to the oxidative effect of W(vi) species in the hydrothermal system.

The morphology and crystal structure of the pristine SnO<sub>2</sub> nanoparticles are further inspected with SEM, TEM and HRTEM, as shown in Fig. S2,† 2a and b. The pristine SnO<sub>2</sub> are composed of nanoparticles with diameter from 6 to 20 nm (Fig. 2a and b) and clear lattice fringes can be identified with layer spacing of 0.334 and 0.262 nm, corresponding to the (110) and (101) diffraction of cassiterite SnO<sub>2</sub>. The TEM image of WS-5 nanoparticles in Fig. 2c indicates that the doped sample WS-5 has a reduced uniform size distribution with diameter of about 6 nm. The HRTEM image in Fig. 2d further shows the lattice fringes of individual WS-5 particles with a layer spacing of 0.334 nm and 0.264 nm rising from the (110) and (101) crystal planes of cassiterite SnO<sub>2</sub> respectively. The observed size distribution and peak assignment agree well with the results from XRD patterns. The STEM-EDX mapping of the WS-5 sample in Fig. 2e–h clearly shows the uniform distribution of O, Sn and W, indicating the good doping effect of W element.

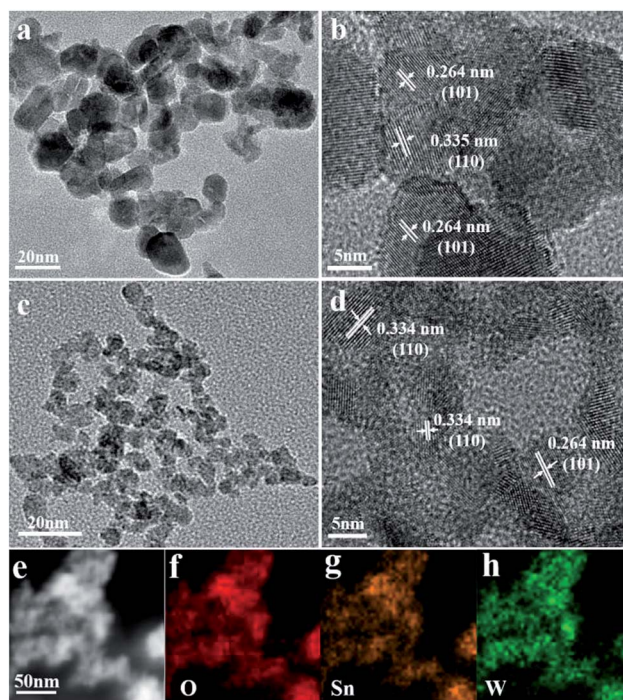


Fig. 2 (a and b) TEM and HRTEM images of pristine SnO<sub>2</sub> nanoparticles WS-0; (c and d) TEM and HRTEM images of doped SnO<sub>2</sub> nanoparticles WS-5; (e) the STEM and (f–h) EDS elemental mapping of WS-5.

The decreased size in SnO<sub>2</sub> nano-crystallite after doping leads to enhanced surface area and more gas adsorption sites, which could improve the sensitivity to the target gas.

The surface chemical states of the pristine SnO<sub>2</sub> and W-doped SnO<sub>2</sub> were examined by X-ray photoelectron spectroscopy (XPS). As shown in the full spectrum survey of Fig. 3a, the Sn 3d, O 1s and W 4f can be detected, confirming the presence of the W component in the WS-5, which is in agreement with the results of EDS mapping. As shown in Fig. 2b, the peaks of W 4f<sub>7/2</sub> at 36.5 eV and W 4f<sub>5/2</sub> at 38.6 eV can be assigned to the existence of the W(VI) chemical state. The O 1s peak at 530.7 eV and 532.0 eV in pristine SnO<sub>2</sub> and WS-5 sample as shown in Fig. 3c. The Sn 3d XPS spectra of WS-0 and WS-5 can be assigned to Sn<sup>4+</sup> of bulk SnO<sub>2</sub>.<sup>32</sup> Note that the two Sn 3d peaks of WS-0 (Sn 3d<sub>3/2</sub> = 495.2 eV, Sn 3d<sub>5/2</sub> = 486.8 eV) are shifted to a lower binding energy in WS-5 (Sn 3d<sub>3/2</sub> = 495.0 eV, Sn 3d<sub>5/2</sub> = 486.6 eV), which are caused by the replacement of Sn<sup>4+</sup> by W<sup>6+</sup> that decreases the binding energy of Sn. The vibration spectra of the samples were further investigated, as is shown in the Raman spectra of Fig. S3.† With the doping of W, the vibration of bond displayed typically decrease in strength, which is caused by the disturbance of the SnO<sub>2</sub> lattice by tungsten incorporation and size reduction. Meanwhile, two peaks arise at 942 cm<sup>-1</sup> and 992 cm<sup>-1</sup>, which are believed to come from the vibration of surface W–O complex.<sup>33</sup>

### 3.2 Gas sensing properties

While gas sensing is based on the charge carrier change caused by the adsorption and desorption events, the gas-sensing performance of the materials are significantly influenced by

the operation temperature. The response of SnO<sub>2</sub> and W-doped SnO<sub>2</sub> towards 10 ppm H<sub>2</sub>S gas were evaluated at different operating temperature from 160 °C to 400 °C and the response gradually decreases with the increasing temperature, as shown in Fig. 4a. At 160 °C, all the doped SnO<sub>2</sub> showed higher response than the pristine one with the highest response of 87 coming from WS-5 (Fig. S4†). Besides sensitivity, response time and recovery time are equally important parameters for designing gas sensors, which are relatively long at low temperature and short at high temperature. Fig. 4b shows the response time and recovery time of WS-0 and WS-5 *versus* 10 ppm hydrogen sulfide over the operating temperature range with complete data for all doped samples shown in Fig. S5.† With most of the response time falling below 50 s, the shortest time of 17 s comes from WS-5 at 260 °C. While the response time of all samples are relatively close and not susceptible to varying temperature, the recovery time of the samples are extremely sensitive to the temperature. No sample is capable of recovering to 90% of the baseline resistance within 300 s at the low temperature of 160 °C, impeding the real-time gas response which requires reasonably fast recovery. Meanwhile, the recovery time of all samples could be decreased significantly by increasing the operating temperature to 260 °C with the best performance of only 7 s from WS-5.

The rapid response and recovery process at 260 °C is due to rapid surface chemistry reaction, higher electron mobility and increased gas diffusion rate. In addition, the formation of oxygen adsorbed at high temperature may be from O<sub>2</sub><sup>-</sup> to O<sup>2-</sup>, O<sub>2</sub><sup>-</sup> + 3e<sup>-</sup> → 2O<sup>2-</sup>(ads).<sup>34</sup> However, further increase in operating temperature could not shorten the response and recovery time significantly, as shown in Fig. 4b. Reduced power

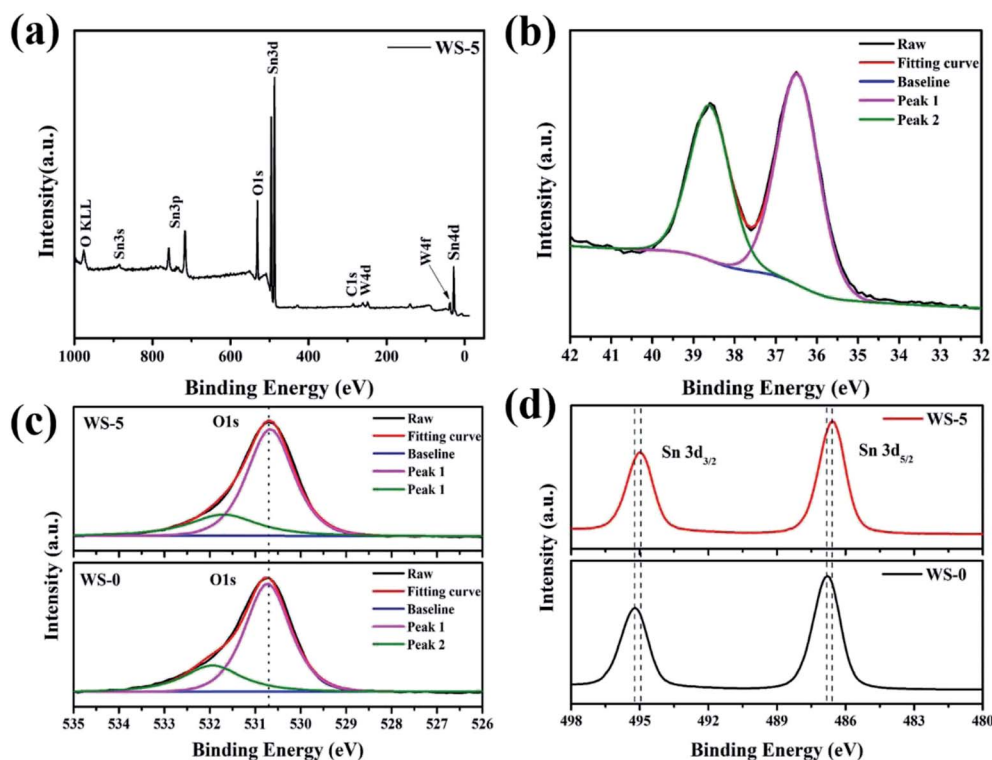


Fig. 3 (a) The full XPS survey graph of WS-5; (b) W 4f XPS spectra of WS-5; (c) XPS O 1s and (d) Sn 3d spectra of WS-0 and WS-5.

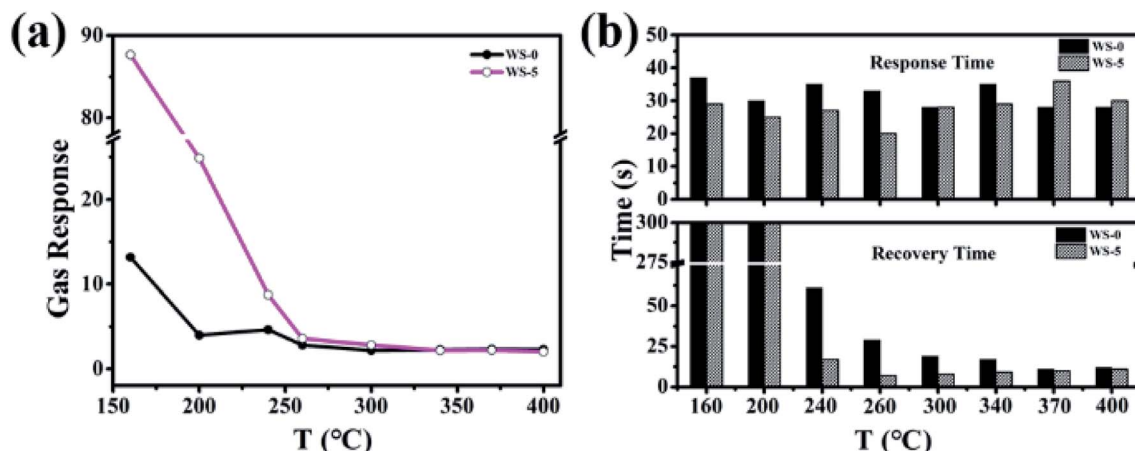


Fig. 4 (a) Gas response of SnO<sub>2</sub> and W-doped SnO<sub>2</sub> to H<sub>2</sub>S at various temperatures from 160 °C to 400 °C; (b) response time and recovery time of the WS-0 and WS-5 nanoparticles upon exposure to 10 ppm H<sub>2</sub>S gas at an operating temperature from 160 °C to 400 °C.

consumption afforded by low temperature and quick response and recovery afforded by high temperature should strike a balance in term of applications in industry. In this considerations, 260 °C was chosen as the optimum operating temperature and WS-5 was chosen as the optimum sample for the following investigation.

The sensing performances of different sensors to H<sub>2</sub>S is summarized in Table 1. As compared to other reports, the W-doped SnO<sub>2</sub> in this report not only significantly decrease respond time and recovery time, but also enhance the SnO<sub>2</sub> based sensor with excellent reversibility and stability.

The typical response and recovery curve of WS-5 to 10 ppm H<sub>2</sub>S at operation conditions was shown in Fig. 5a with a response time of 17 s and recovery time of 7 s, respectively. The response of WS-5 to different concentrations of hydrogen sulfide was shown in Fig. 5b, with the lowest concentration at 100 ppb, indicating the low detection limit of the material. For practical application, robustness and stability of the sensor is the most important factor to be considered. Materials need to be inactivate at H<sub>2</sub>S atmosphere. The response of WS-5 to 10 ppm H<sub>2</sub>S become stable after 10 cycles as shown in Fig. S6.† The sensing stability of WS-5 was evaluated at 260 °C by repetitive injection of 10 ppm H<sub>2</sub>S and exposure to air during which the resistance of the sensing materials was recorded. As is shown in Fig. 5c and d, the sensor retains constant response and resistance through 40 cycles of H<sub>2</sub>S injection and air exposure with no sign of performance degradation. In contrast,

the gas response of WS-0 varies significantly and the baseline resistance reading is hard to stabilize within the first 40 cycles. Furthermore, the long-term stability of WS-5 was also investigated. As can be seen in Fig. S7,† WS-5 shows excellent stability in the daily cycle test, and the sensitivity to H<sub>2</sub>S remains almost unchanged during the 10 day evaluation period.

As shown in Fig. 6, the response of WS-0 and WS-5 to hydrogen (100 ppm), ammonia (10 ppm), methane (2000 ppm), and carbon monoxide (100 ppm) is compared at the same temperature of 260 °C. Both WS-0 and WS-5 show no response to methane and carbon monoxide, and smaller response to 100 ppm of hydrogen and 10 ppm of ammonia. In addition, WS-5 shows an improved selectivity to hydrogen sulfide than to the other gases.

### 3.3 The gas sensing mechanism

Based on the above results, the morphology and structure of the material have deep impact on the response to the adsorbed gas. The morphology of W-doped SnO<sub>2</sub> has changed significantly with the particles size decreasing from 15 nm to 6 nm, providing more specific area. In addition, the surface-adsorption induced charge-depletion will lead to increased ratio of charge-depletion volume and more significant variation of the resistance upon sensing. Therefore, the increase in gas sensitivity of WS-5 is mainly attributed to tungsten doping.<sup>41</sup> Besides, the XRD patterns from all samples with doping level of 1% to 10% do not show the presence of tungsten oxide phase,

Table 1 Comparison of H<sub>2</sub>S sensing performance of several doped metal oxide sensors

Materials	Concentration (ppm)	Response ( $R_a/R_g$ )	Working temperature (°C)	$t_{res}/t_{rec}$ (s)	Ref.
SnO <sub>2</sub> nanocrystals	5	1.6	275	15/62	35
Au-SnO <sub>2</sub> hollow spheres	5	17.4	400	18/—	36
Au-embedded WO <sub>3</sub> nanowire	10	18	291	27/230	37
Au-SnO <sub>2</sub> NTs	5	34	300	~35/—	38
rGO-SnO <sub>2</sub> NFs	5	33.7	200	~115/~110	39
Mo-doped ZnO nanowires	5	14	300	20/223	40
W-SnO <sub>2</sub>	10	3.6	260	17/7	This work

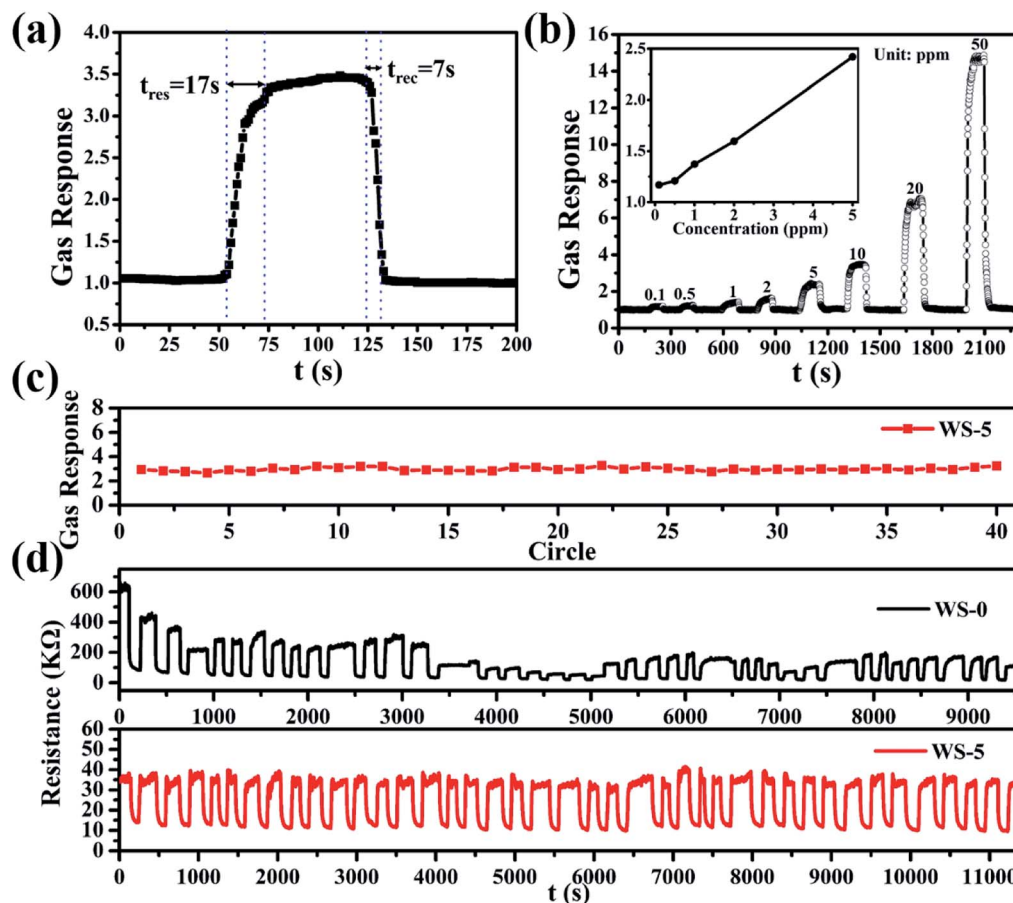


Fig. 5 (a) Real-time gas sensing transients of the sensor based on WS-5 to 10 ppm  $\text{H}_2\text{S}$  at 260 °C; (b) gas response of WS-5 to various concentration  $\text{H}_2\text{S}$  gas ranging from 0.1 ppm to 50 ppm; (c) gas-response reading of the sensor based WS-5 to 10 ppm  $\text{H}_2\text{S}$  at 260 °C; (d) 40 cycles of the sensor based on WS-0 and WS-5 to 10 ppm  $\text{H}_2\text{S}$  at 260 °C.

indicating that  $\text{W}^{6+}$  is doped into the lattice of  $\text{SnO}_2$ , thanks to the similar ion radius of  $\text{W}^{6+}$  and  $\text{Sn}^{4+}$ . The aliovalent doping creates abundant adsorption sites on the surface of  $\text{SnO}_2$  for  $\text{O}_2$

and  $\text{H}_2\text{S}$ , and induced further change in the band structure which may also contribute to the faster adsorption/desorption.<sup>42</sup>

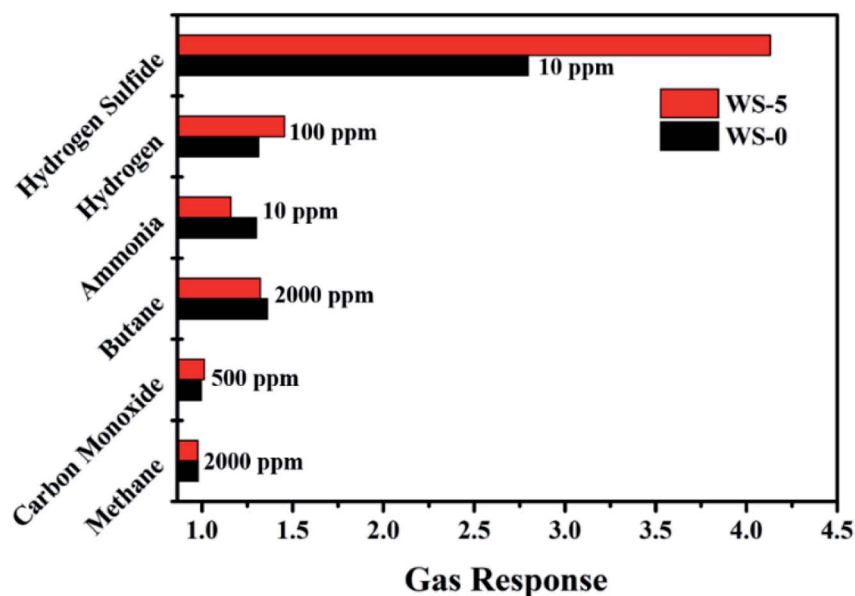
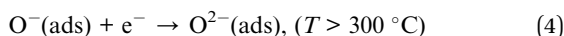
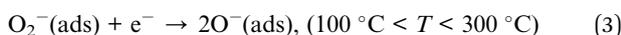
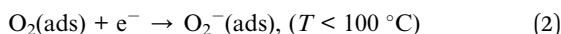
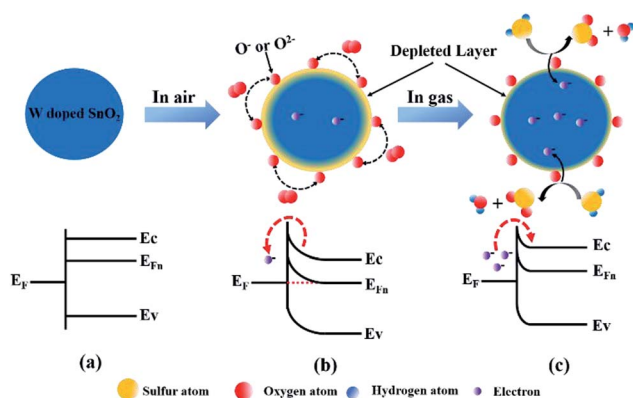


Fig. 6 Response of WS-0 and WS-5 sensor exposed to several gases at 260 °C.

As a typical n-type semiconductor, the band structure of SnO<sub>2</sub> is not altered from the flat-band situation when there is no electron transfer between the adsorbed molecules and the conduction band at the surface, as shown in Scheme 1a. According to the surface-depletion model, chemisorption of oxygen (O<sub>2</sub>) on the surface of sensing materials upon exposure to the air extracts the free electrons from the conduction band and traps them at the surface by forming chemisorbed oxygen species (O<sub>2</sub><sup>-</sup>, O<sup>-</sup>, O<sup>2-</sup>),<sup>42,43</sup> as shown in Scheme 1b. This would result in the formation of a space-charge layer and upward band bending near the surfaces. The potential barrier increases *via* restricting the flow of electrons.<sup>41</sup> Different types of oxygen uptake depend on the operating temperature. When the temperature is lower than 100 °C, O<sub>2</sub><sup>-</sup> usually undergoes chemical reactions. However, when the temperature ranges from 100 to 300 °C, O<sup>-</sup> becomes a common chemical reaction and O<sup>2-</sup> disappears rapidly. Oxygen species mainly exist in the form of O<sup>2-</sup> when the temperature exceeds 300 °C.<sup>44</sup> The reaction can be described by the following steps.<sup>45-47</sup>



At the operating temperature of 260 °C, the mainly adsorbed oxygen are O<sub>2</sub><sup>-</sup> and O<sup>-</sup>. Once the sensor was exposed to the H<sub>2</sub>S gas, these adsorbed oxygen (O<sub>2</sub><sup>-</sup>, O<sup>-</sup>) would react with H<sub>2</sub>S molecules to form SO<sub>2</sub> and water vapor. In this process, the captured electrons are released back into the depletion layer. Therefore, the depletion layer will shrink and the resistance of WS-5 reduced (Scheme 1c). This chemical reaction can be described below:



Scheme 1 Schematic images and band diagrams of the surface reactions in different atmosphere: (a) in Ar; (b) exposed to air; (c) in air with the presence of H<sub>2</sub>S gas. E<sub>c</sub>: conduction band; E<sub>F</sub>: redox potential of adsorbed molecules; E<sub>Fn</sub>: Fermi level in the n-type semiconductor; E<sub>v</sub>: valence band.

Adsorbed oxygen ions (O<sub>2</sub><sup>-</sup>, O<sup>-</sup> or O<sup>2-</sup>) are known to be the most common surface species in SMOs.<sup>28</sup> The introduction of aliovalent tungsten atoms actually increase the conductivity by further modifying the electronic band structure of SnO<sub>2</sub> and hence improves the reversibility of H<sub>2</sub>S adsorption and desorption, which in turn improves the H<sub>2</sub>S durability of the sensor. As for the asymmetric variation of response and recovery time with the temperature, it is attributed to the different pathways in adsorption and desorption. A series of complicated processes will take place which can be briefly divided into gas-phase diffusion and surface-reaction. The kinetics of a tandem process is usually determined by the rate of the slowest reaction which may differ in the response and recovery process.<sup>48</sup> However, our discussion is far from satisfactory and further experiments are needed to fully illustrate the picture behind the complicated sensing behavior.

## 4. Conclusions

A simple hydrothermal method was used to obtain W-doped tin dioxide nanoparticles of about 6 nm. In the operating temperature from 160 °C to 400 °C, 5% W-doped SnO<sub>2</sub> shows the best response to 10 ppm H<sub>2</sub>S at 260 °C. The synergistic effect of tungsten doping and size reduction of SnO<sub>2</sub> crystallites have a great influence on the structure and gas performance of the materials. Compared with pristine SnO<sub>2</sub>, 5% W-doped SnO<sub>2</sub> exhibits enhanced gas sensitivity down to 100 ppb of H<sub>2</sub>S while the response time and recovery time can be reduced to 17 s and 7 s, respectively. Most importantly, the W-doped SnO<sub>2</sub> shows an extraordinary stability with almost unchanged baseline resistance and response resistance after 40 circles and 10 days tested. The enhanced gas sensing performance is mainly due to the decreased particle size of W-doped SnO<sub>2</sub>, increased specific surface area and the doping-modified electronic structure. We hope our endeavor in the highly-durable H<sub>2</sub>S sensor will provide useful guidance for the other gas-sensing materials with extraordinary performance for industrial applications.

## Conflicts of interest

There are no conflicts to declare.

## Acknowledgements

This work was financially supported by the National Science Foundation of China under No. 21601133, 21676215 and 61701543, China Postdoctoral Science Foundation (2018M633556) and Sinopec Innovation Scheme under A-381.

## Notes and references

- 1 D. Yang, G. Chen and R. Zhang, *Aerosol Air Qual. Res.*, 2006, **6**, 430–443.
- 2 S. K. Pandey, K. H. Kim and K. T. Tang, *Trends Anal. Chem.*, 2012, **32**, 87–99.

- 3 Z. Gao, D. Tang, D. Tang, R. Niessner and D. Knopp, *Anal. Chem.*, 2015, **87**, 10153–10160.
- 4 M. Malekalaie, M. Jahangiri, A. M. Rashidi, A. Haghghiasl and N. Izadi, *Mater. Sci. Semicond. Process.*, 2015, **38**, 93–100.
- 5 M. Govindhan, B.-R. Adhikari and A. Chen, *RSC Adv.*, 2014, **4**, 63741–63760.
- 6 Y. Nie, P. Deng, Y. Zhao, P. Wang, L. Xing, Y. Zhang and X. Xue, *Nanotechnology*, 2014, **25**, 265501.
- 7 J. Shu, Z. Qiu and D. Tang, *Anal. Chem.*, 2018, **90**, 9691–9694.
- 8 P. G. Su and Y. T. Peng, *Sens. Actuators, B*, 2014, **193**, 637–643.
- 9 D. R. Miller, S. A. Akbar and P. A. Morris, *Sens. Actuators, B*, 2014, **204**, 250–272.
- 10 D. H. Kim, J. S. Jang, W. T. Koo, S. J. Choi, H. J. Cho, M. H. Kim, S. J. Kim and I. D. Kim, *ACS Sens.*, 2018, **3**, 1164–1173.
- 11 Y. Fu, Y. Zhao, P. Wang, L. Xing and X. Xue, *Phys. Chem. Chem. Phys.*, 2014, **17**, 2121–2126.
- 12 J. Kim and K. Yong, *J. Phys. Chem. C*, 2011, **115**, 7218–7224.
- 13 S. C. Lee, B. W. Hwang, S. Y. Kim, J. H. An, S. Y. Jung, J. S. Huh, D. D. Lee and J. C. Kim, *J. Nanoelectron. Optoelectron.*, 2015, **10**, 460–465.
- 14 Y. Wang, B. Liu, S. Xiao, X. Wang, L. Sun, H. Li, W. Xie, Q. Li, Q. Zhang and T. Wang, *ACS Appl. Mater. Interfaces*, 2016, **8**, 9674–9683.
- 15 Q. Zhou, W. Chen, L. Xu, R. Kumar, Y. Gui, Z. Zhao, C. Tang and S. Zhu, *Ceram. Int.*, 2018, **44**, 4392–4399.
- 16 G. J. Sun, S. W. Choi, A. Katoch, P. Wu and S. K. Sang, *J. Mater. Chem. C*, 2013, **1**, 5454–5462.
- 17 S. J. Choi, C. Choi, S. J. Kim, H. J. Cho, M. Hakim, S. Jeon and I. D. Kim, *Sci. Rep.*, 2015, **5**, 8067.
- 18 K.-I. Choi, H.-J. Kim, Y. C. Kang and J.-H. Lee, *Sens. Actuators, B*, 2014, **194**, 371–376.
- 19 Z. Song, Z. Wei, B. Wang, Z. Luo, S. Xu, W. Zhang, H. Yu, M. Li, Z. Huang, J. Zang, F. Yi and H. Liu, *Chem. Mater.*, 2016, **28**, 1205–1212.
- 20 Z. Li, N. Wang, Z. Lin, J. Wang, W. Liu, K. Sun, Y. Q. Fu and Z. Wang, *ACS Appl. Mater. Interfaces*, 2016, **8**, 20962–20968.
- 21 Y. Sun, S. Gao, F. Lei and Y. Xie, *Chem. Soc. Rev.*, 2015, **44**, 623–636.
- 22 J. Shu, Z. Qiu, Q. Zhou and D. Tang, *Chem. Commun.*, 2019, **55**, 3262–3265.
- 23 H. Zhang, *ACS Nano*, 2015, **9**, 9451–9469.
- 24 U. N. Maiti, W. J. Lee, J. M. Lee, Y. Oh, J. Y. Kim, J. E. Kim, J. Shim, T. H. Han and S. O. Kim, *Adv. Mater.*, 2014, **26**, 40–67.
- 25 L. Peng, X. Peng, B. Liu, C. Wu, Y. Xie and G. Yu, *Nano Lett.*, 2013, **13**, 2151–2157.
- 26 Y. Al-Hadeethi, A. Umar, S. H. Al-Heniti, R. Kumar, S. H. Kim, X. Zhang and B. M. Raffah, *Ceram. Int.*, 2017, **43**, 2418–2423.
- 27 Y. Huang, G. Li, J. Feng and Q. Zhang, *Thin Solid Films*, 2010, **518**, 1892–1896.
- 28 J. Hu, T. Wang, Y. Wang, D. Huang, G. He, Y. Han, N. Hu, Y. Su, Z. Zhou and Y. Zhang, *Sens. Actuators, B*, 2018, **263**, 120–128.
- 29 Z. Dai, L. Xu, G. Duan, T. Li, H. Zhang, Y. Li, Y. Wang, Y. Wang and W. Cai, *Sci. Rep.*, 2013, **3**, 1669.
- 30 W. Zhang, X. L. Cheng, X. Zhang, Y. Xu, S. Gao, H. Zhao and L. Huo, *Sens. Actuators, B*, 2017, **247**, 664–672.
- 31 X. Liu, N. Chen, B. Han, X. Xiao, G. Chen, I. Djerdj and Y. Wang, *Nanoscale*, 2015, **7**, 14872–14880.
- 32 S. Cui, Z. Wen, E. Mattson, S. Mao, J. Chang, M. Weinert, C. Hirschmugl, M. Gajdardzikajosiifovska and J. Chen, *Mater. Sci. Eng., C*, 2013, **1**, 4462–4467.
- 33 A. A. El-Kheshen, F. H. El-Batal and S. Y. Marzouk, *Indian J. Pure Appl. Phys.*, 2008, **46**, 225–238.
- 34 Y. Wang, B. Liu, S. Xiao, H. Li, L. Wang, D. Cai, D. Wang, Y. Liu, Q. Li and T. Wang, *J. Mater. Chem. A*, 2015, **3**, 1317–1324.
- 35 M. Lin, Y. Chen and J. Ma, *Sci. Rep.*, 2014, **4**, 6028.
- 36 S. J. Choi, M. P. Kim, S. J. Lee, B. J. Kim and I. D. Kim, *Nanoscale*, 2014, **6**, 11898–11903.
- 37 N. Minh Vuong, D. Kim and H. Kim, *Sci. Rep.*, 2015, **5**, 11040.
- 38 J.-S. Jang, S.-J. Kim, S.-J. Choi, N.-H. Kim, M. Hakim, A. Rothschild and I.-D. Kim, *Nanoscale*, 2015, **7**, 16417–16426.
- 39 S.-J. Choi, B.-H. Jang, S.-J. Lee, B. K. Min, A. Rothschild and I.-D. Kim, *ACS Appl. Mater. Interfaces*, 2014, **6**, 2588–2597.
- 40 H. S. Woo, C. H. Kwak, I. D. Kim and J. H. Lee, *J. Mater. Chem. A*, 2014, **2**, 6412–6418.
- 41 J. Shu, Z. Qiu, S. Lv, K. Zhang and D. Tang, *Anal. Chem.*, 2017, **89**, 11135–11142.
- 42 Z. Li, Y. Huang, S. Zhang, W. Chen, K. Zhong, D. Ao, L. Wei and Y. Fu, *J. Hazard. Mater.*, 2015, **300**, 167–174.
- 43 L. Xu, R. Xing, J. Song, W. Xu and H. Song, *J. Mater. Chem. C*, 2013, **1**, 2174–2182.
- 44 C. Shoou-Jinn, H. Ting-Jen, C. I-Cherng and H. Bohr-Ran, *Nanotechnology*, 2008, **19**, 175502.
- 45 X. Kou, C. Wang, M. Ding, C. Feng, X. Li, J. Ma, H. Zhang, Y. Sun and G. Lu, *Sens. Actuators, B*, 2016, **236**, 425–432.
- 46 W. Yang, P. Wan, X. Zhou, J. Hu, Y. Guan and L. Feng, *Sens. Actuators, B*, 2014, **201**, 228–233.
- 47 H. Liu, S. P. Gong, Y. X. Hu, J. Q. Liu and D. X. Zhou, *Sens. Actuators, B*, 2009, **140**, 190–195.
- 48 Z. Boroun, M. Ghorbani, A. Moosavi and R. Mohammadpour, *J. Phys. Chem. C*, 2016, **120**, 7678–7684.